Nano-captured water affects the wettability of cellulose nanofiber films

Misaka, Masumi
Department of Aeronautics and Astronautics, Kyushu University

Teshima, Hideaki
Department of Aeronautics and Astronautics, Kyushu University

Hirokawa, Sota
Department of Aeronautics and Astronautics, Kyushu University

Li, Qin-Yi
Department of Aeronautics and Astronautics, Kyushu University

他

出版情報：Surfaces and Interfaces. 46, pp.103923-, 2024-03. Elsevier
バージョン：
権利関係：

Nano-captured Water Affects the Wettability of Cellulose Nanofiber Films

Masumi Misaka[1], Hideaki Teshima[1,2], Sota Hirokawa[1,2], Qin-Yi Li[1,2], Koji Takahashi[1,2]*

[1] Department of Aeronautics and Astronautics, Kyushu University, 744 Motooka, Nishi-Ku, Fukuoka 819-0395, Japan

[2] International Institute for Carbon-Neutral Energy Research (WPI-I2CNER), Kyushu University, 744 Motooka, Nishi-Ku, Fukuoka 819-0395, Japan

* Corresponding author: Postal address: 744 Motooka, Nishi-Ku, Fukuoka 819-0395, Japan, Tel.: +81-92-802-3016; Fax: +81-92-802-3017; Email: hteshima05@aero.kyushu-u.ac.jp

Email

Masumi Misaka: misaka.masumi.489@s.kyushu-u.ac.jp

Hideaki Teshima: hteshima05@aero.kyushu-u.ac.jp

Sota Hirokawa: hirokawa.sota.807@s.kyushu-u.ac.jp

Qin-Yi Li: qinyi.li@aero.kyushu-u.ac.jp

Koji Takahashi: takahashi@aero.kyushu-u.ac.jp

Highlights

- Wettability of cellulose nanofiber (CNF) films depends on the thickness.
- CNF networks retain water even under ultra-high vacuum conditions of 10^{-5} Pa.
- Thick CNF films can retain water but thin ones cannot.
- Amount of water content within the CNF films affects their wettability.
- The minimum thickness at which CNF films could retain water is 68 nm.

Abstract

In this study, we report that the wettability of cellulose nanofiber films varies with their thickness, and this variation is attributed to the amount of water captured within the hydrogel-like film. To investigate this, we conducted water contact angle measurements on cellulose nanofiber films with different thicknesses. The wettability of the films was found to change from hydrophilic (approximately 20°) to that of the underlying silicon substrate (approximately 80°) by decreasing the mean film thickness within a range of 150 nm or less. Transmission electron microscope observations revealed that even under high-vacuum conditions ($< 10^{-5}$ Pa), water was captured in regions where the film was thick

enough to form a dense, three-dimensional network. However, in regions where the film was thin, the network structure became sparse and two-dimensional, and no water was observed. We propose that the wettability of cellulose nanofiber films changes based on the area ratio of water captured in thick 3D network regions, the underlying substrate, and the cellulose nanofiber. Furthermore, we quantitatively evaluated the relationship between the area ratio and the wetting state of the composite surface based on the Cassie-Baxter equation, then determined the minimum thickness at which water is retained within the cellulose fiber network.

Keywords

Cellulose nanofibers, Hydrogel, Wettability, Transmission electron microscopy, the Cassie-Baxter equation

1. Introduction

Wetting is a familiar phenomenon commonly observed in both industry and our daily life [1–4], and is of great significance both in fundamental scientific research and in a wide range of engineering applications, such as anti-fogging [5,6], anti-fouling surfaces [7], phase-change heat transfer [8] and water/oil separation [9,10]. Thus, scientific effort has been devoted to controlling wettability [11], using approaches that include chemical modification, fabrication of micro- and nanostructures, lubricant infusion, and film coating. Among these approaches, the use of nanomaterials and their composite films is particularly promising. For example, depositing hydrophilic nanoparticles on the target surfaces or films (or mixing the nanoparticles with them) has become a common method to adjust their wettability [12–18]. The mechanism by which this influences the wettability is a combination of an increase in surface roughness by the exposure to the nanoparticles and the creation of a hydrophilic–hydrophobic hybrid surface.

In addition to nanoparticles (which are zero-dimensional materials), various types of one-dimensional (1D) nanomaterial (such as nanotubes, nanorods, and nanowires) and two-dimensional (2D) nanomaterials (such as nanosheets and nanoribbons) exist. Recent studies have reported that these nanomaterials can produce films with unique properties. For example, a film composed of pristine carbon nanotubes was shown to change its wettability from superhydrophobic to superhydrophilic upon temperature change [19], which may be due to the conversion of electrical behavior from semiconducting to metallic [20]. Thus, developing and characterizing new films that take advantage of nanomaterials for further control of wetting phenomena are highly desirable.

Among the various nanomaterials available, we chose to focus on wettability control using nanofibers. Some studies have focused on films and membranes using nanofibers [21–23]. In general, nanofiber

films are prepared by electrospinning, in which they are generated by applying a high voltage to a polymer solution in a spinning nozzle [24]. Several ways exist to alter the wettability of nanofiber membranes. For example, Arslan et al. introduced perfluoro alkoxysilanes into electrospun cellulose acetate nanofibers to convert them to hydrophobic, and then applied them to nanofiber mats for oil/water separation [25]. Huang et al. fabricated a super-amphiphobic membrane with anti-surfactant-wetting characteristics by coaxial electrospinning and improved the performance of membrane distillation [26]. In addition to such chemical surface treatment, a change in surface structure can also shift the wettability of a nanofiber mat. For example, Benito et al. controlled the wettability of carbon nanofiber layers on a nickel foil by varying the surface roughness, porosity, and layer thickness [27].

We suggest that cellulose nanofibers (CNFs) could be an effective candidate for controlling wettability in a simpler way than previously described techniques. Cellulose nanofibers, which are the most abundant polymeric 1D materials on earth, have recently attracted increasing attention as environmentally friendly biodegradable nanomaterials [28–30]. They are hydrophilic because of hydroxyl groups along their molecular chain [31] thus, films composed of their three-dimensional (3D) networks behave as a hydrogel by capturing water in nanoscale spaces [32,33]. In addition to their inherent hydrophilic properties, their surface properties (such as their wettability) can be modified by introducing functional groups to their molecular chain [34–36]. Thus, there are some studies on composite and coating membranes utilizing CNF [37,38]. For example, Cai et al. manufactured an excellent water/oil separation membrane by alternately spraying chitosan solution and CNF dispersion onto a laboratory filter membrane, utilizing spray-assisted layer-by-layer (LBL) assembly technology [39]. Jamaluddin et al. demonstrated that incorporating CNFs, which were first acylated and then propionylated, into poly(lactic acid) (PLA) resulted in the successful creation of a composite film with enhanced wettability [40]. However, although some studies have investigated the wettability of CNF-

based composite or coated films, the characterization of the wetting properties of pure CNF films, which is most fundamental and important for the future application of CNFs, has rarely been studied. In this study, we investigated the wettability of pure CNF films deposited on silicon substrates and found that their wettability deteriorates and approaches that of the underneath silicon substrate when the mean film thickness is less than about 150 nm. Furthermore, using transmission electron microscopy (TEM), we revealed that CNF films consisted of water-captured (i.e. hydrogel) regions and non-water-captured regions. On the basis of these results, we discuss the mechanism of wettability variation of CNF films with thickness.

2. Experiment

2.1 Materials

CNFs were purchased from Cellulose Lab (Canada.). The crystallinity of the CNFs was estimated to be 56.3% (see Supplementary Material, Note 1). Silicon wafer was purchased from SUMITOMO SHOJI CHEMICALS CO., LTD. (Japan). Acetone (99.7 %) was purchased from KISHIDA CHEMICAL Co.,Ltd. (Japan).

2.2 Fabrication of CNF films

The following procedure was used to form CNF films with different thicknesses on silicon substrates (Fig. 1(a)). First, freeze-dried unmodified cellulose nanofibers were added to pure water to prepare CNF dispersion solutions of different concentrations. The dispersion solutions were sonicated using an ultrasonic disperser (UP400S, Hielscher, Germany) for 1 hour. Next, the silicon wafer was cleaned with acetone, rinsed with pure water, and then dried with nitrogen gas to remove any contaminants. Pure water was prepared using a water purifier (RFP742HA, Advantec, Japan). The wafer was cut into 4 cm × 4 cm size and placed on hydrophobic Teflon sheets larger than the pieces. To create CNF films on silicon substrates, CNF dispersion solution (1 mL) was dropped onto the wafer and dried at 90°C for 1.5 hours. By adjusting the concentration and amount of the solution, samples with film thicknesses ranging from 9 to 650 nm were prepared. All processes were conducted in a cleanroom where temperature (296 K) and humidity (55%) were controlled.

2.3 Measurement of contact angles

The wettability of the CNF films was characterized by measuring the contact angle of a 1 μL water droplet on the surface. The contact angles were measured from the cross-sectional image of the droplets captured using a CCD camera. It should be noted that the droplets were put on the center area of the films, namely, a macroscopically uniform surface, to avoid the coffee-ring effect of the CNFs. Moreover, we found that wicking occurs after droplet deposition due to the surface roughness and finishes within five seconds at most. Thus, to eliminate the influence of this transient phenomenon, contact angle measurements were conducted after the wicking had finished, specifically 10 seconds following the deposition of the droplet. Furthermore, the droplet size was set at 1 μL for the following reasons. Yan et al. reported that contact angle measurements using small droplets of 2 μL with a goniometer were consistent with the values reported by a microgoniometer [41]. It is also widely known that when the radius of the liquid-gas interface of a droplet is smaller than the capillary length (which is about 2.7 mm for water and air), the droplet becomes distorted due to the influence of gravity [42]. Moreover, the base area of the droplet must be substantially larger than the scale of chemical and structural heterogeneity on the surface. Based on these references, we chose the 1 μL droplet in our contact angle measurements. In addition, all processes were conducted in a cleanroom where temperature (296 K) and humidity (55%) were controlled. We note that although our contact angle measurements are limited in a standard environment, their dependence on conditions such as humidity and temperature should be noted. Further characterization of the effect of specific conditions on the wettability is beyond the scope of this article and will be explored in future works.

2.4 Measurement of thickness of CNF films

142 The mean thickness of the CNF films was evaluated by averaging the profiles obtained by a stylus
143 profiling system (DektakXT, Bruker, USA). Notably, because the large tip radius of the stylus head
144 (12.5 μm) results in an overestimation of the lateral profile of the spike-like geometry, such regions
145 were excluded from the averaging as errors.

146

147 2.5 Measurement of thickness distribution in CNF films

148 Furthermore, to obtain a thickness distribution of CNF films, coherence scanning interferometry (CSI;
149 VS1330, HITACHI, Japan) was used. Samples for CSI measurements were prepared as follows. Glass
150 slides were used as substrates instead of silicon substrates because they are the only applicable material
151 for film-thickness measurements using CSI because of their high transparency. First, a 1 cm × 1 cm
152 Teflon sheet with an 8-mm-diameter hole at the center was put onto a glass slide. Next, 80 μL of CNF
153 dispersion solution was dropped into the central hole. Then, the film was formed by drying at 90°C for
154 1.5 hours. This procedure was repeated for different glass slides using different concentrations of
155 dispersion solution to create samples with different thicknesses. Then, we were able to obtain their mean
156 thickness and 3D height distribution (histogram) over an area of 1024 μm × 1024 μm using CSI. It was
157 assumed that the CNF thickness distribution on the glass slides was the same as that on the silicon
158 substrates. In addition, alongside the acquisition of the film thickness distribution, the specific surface
159 area was obtained.

160

161 2.6 TEM observation of CNF films

We also observed a CNF film using TEM. First, a droplet of 0.25-wt% CNF dispersion solution was placed onto a TEM grid (Cu-2000HS, Gilder Grids Ltd., UK) and vacuumed for 10 hours at 10^{-3} Pa. The sample was then fixed to a TEM holder and observed with JEM-2100Plus (JEOL Ltd., Japan) at an acceleration voltage of 200 kV. The TEM chamber pressure was approximately 10^{-5} Pa. In addition, to confirm the purity of CNFs, elemental analysis was performed using Energy-dispersive X-ray Spectroscopy (EDS) (See Supplementary Material, Note 2).

3. Results and Discussion

3.1 Wetting behavior of CNF Films as a function of film thickness

In this study, we investigated the relationship between the wettability and thickness of CNF films created on silicon substrates (Fig. 1(a)). Since the film exhibits a nanoscale distribution as shown in Fig. 1(b), we adopted the mean thickness. Fig. 1(c) illustrates the relationship between the mean thicknesses and apparent contact angles of CNF films. The contact angle of the pristine silicon substrate was 80.3 ± 3.2°, which was consistent with the value previously reported [43]. As the graph demonstrates, the CNF films consistently exhibited lower contact angles than that of the silicon substrate. When the mean film thickness was over 150 nm, the contact angle remained almost constant at approximately 20°. By contrast, when the thickness was below 150 nm, the contact angle varied between 15° and 65°, approaching the contact angle of the underlying silicon substrate as the thickness decreased. These findings challenge the conventional understanding that the wettability of a film is uniquely determined by its surface properties and is independent of its thickness. Moreover, based on the relationship between the mean film thicknesses and contact angles, the following empirical formula was derived: $\theta = 59.8e^{-0.03T} + 20.5$. Here, θ [deg.] is a contact angle, T [nm] represents the mean film thickness,

and the R-squared value was 0.79. The convergent value of the contact angle was 20.5°, which corresponds to the average value of the contact angle for CNF films with a thickness greater than 150 nm.

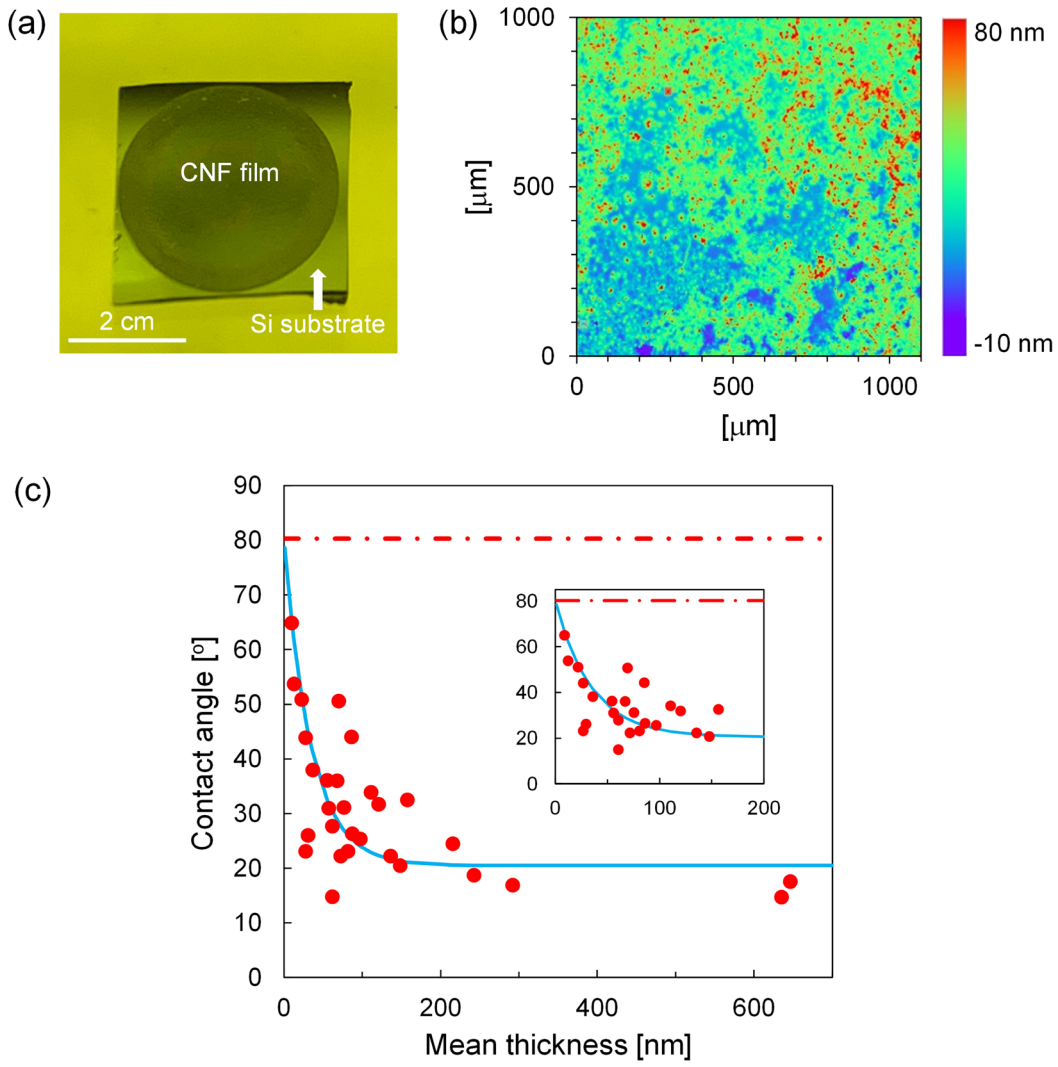

Fig. 1. (a) Photograph of a CNF film formed on a silicon substrate. (b) Thickness distribution of a CNF film with a mean thickness of 37.8 nm measured by CSI. (c) Relationship between the mean thicknesses and contact angles of CNF films. The red dashed lines show the water contact angle on the pristine

192 silicon substrate. The blue solid lines represent an empirical formula: $\boldsymbol{\theta = 59.8e^{-0.03T} + 20.5}$. An
193 enlarged view of the region of low mean thickness is shown as an inset.

194

195

196 3.2 TEM and STEM observation of CNF films

197 To investigate the cause of the contact-angle change, the detailed structures of CNF films were observed
198 by TEM. As shown in Fig. 2(a), the entire region of the films appeared hazy, and individual CNFs were
199 not clearly observed at 0 s; however, with observation time, the image became clearer (Fig. 2(b)).
200 Furthermore, the CNF networks gradually expanded from 0 to 2.4 s. These changes were induced by the
201 irradiation of the electron beam. The electron beam causes the radiolysis of water, leading to the
202 decomposition of water into hydrogen, oxygen, and radicals [44]. Nanobubbles composed of these
203 products have been reported to form during TEM observation [45,46]. Therefore, we speculate that the
204 expansion of the network structures with time is a result of bubble nucleation induced by the radiolysis
205 of the nano-captured water in the CNF network. It is worth clarifying that the water was exposed to a 10^{-5}
206 Pa environment for more than 20 minutes before Fig. 2 was taken, and bubbles did not form before
207 electron beam irradiation. Moreover, Grogan et al. reported that the temperature rise of water under a
208 typical TEM experiment is less than 4 K [47]. Therefore, the heating due to the electron beam is unlikely
209 to cause the boiling. It was noted that bubble nucleation due to the radiolysis has been frequently
210 observed in TEM observation. For example, Hirokawa et al. have observed radiolysis-oriented bubbles
211 in 10 nm thick water [48,49]. Therefore, these results support the conclusion that bubbles were nucleated
212 because of radiolysis.

213

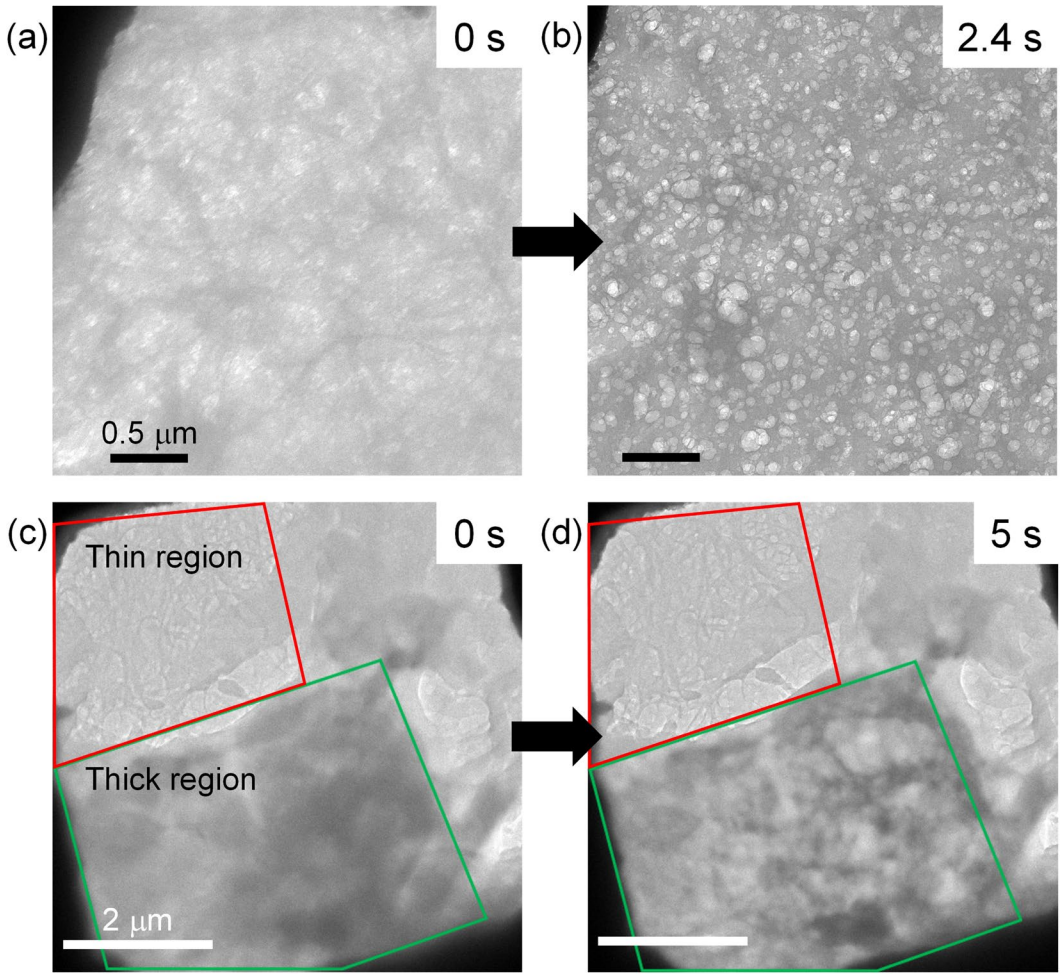

Fig. 2. (a, b) Time series of radiolysis of water captured in CNF networks observed by TEM. (c, d) Time series of a CNF film composed of thin and thick regions. The regions in the red and green squares correspond to the thin and thick regions, respectively.

To investigate the relationship between the film thickness and the water-retention capacity, we observed a CNF film region where thin (red square) and thick (green square) regions coexisted (Fig. 2(c, d)). The area enclosed by the green square was considered to represent a thicker film for the following two reasons. First, when focusing on the area within the red square, the green region appeared blurred,

indicating different heights for their two regions. Second, the contrast in the green square was darker than the red region, indicating that the amount of the transmitted electron beam was lower than that in the red square because of the high molecular density. Consequently, the CNF film in the green frame was thicker than the one in the red square. Furthermore, when electron beams continued to irradiate the entire area, radiolysis of water occurred in the green region, but there was no observable change in the red frame. These results suggest that a certain thickness is necessary to retain water in the hydrogel film. This may be because, when the film is too thin, the network structure fails to form a 3D configuration, thereby preventing the creation of nanoscale spaces essential for water retention. Fig. S5 (see Supplementary Material, Note 3) also shows that radiolysis did not happen when the CNFs were sparsely distributed in the sample. Incidentally, the TEM images were captured after exposing CNFs to the electron beam and allowing more than 30 s to pass without any noticeable changes. This confirmed that the CNFs themselves were not damaged under our observation condition. Additionally, from the TEM images in Fig. S5, 30 fibers were randomly selected, and their diameters were measured. Their diameters ranged from 5.4 to 67.4 nm, with an average of 37.2 nm.

CNF films were observed using both TEM mode and scanning transmission electron microscope (STEM) mode. In TEM mode, the electron beam uniformly irradiates the field of view; by contrast, in STEM mode, the electron beam is converged to a focal point and scans in lines over samples to take scanning images. Fig. 3 shows STEM images of the CNF film before and after the specific areas marked by the yellow dashed frames are irradiated by the focused electron beam. We note that, because we used the annular dark-field (ADF)-STEM mode, which creates images by collecting scattered electrons, an area with brighter contrast corresponds to a higher density area. In contrast with Fig. 3(a), which was imaged before the high-intensity electron beam scanning, the three-dimensional structures of the CNFs

247 became clear only in the beam-irradiated area (Fig. 3(b)). This suggested that water existed in the hazy
248 region and disappeared owing to the radiolysis of water caused by intensive scanning, which was
249 consistent with the results shown in Fig. 2. Furthermore, after 30 s, the region within the dashed lines
250 did not become hazy again, which indicated that water, firmly captured in the gel structure through
251 hydrogen bonding, is in a unique state distinct from the bulk, having lost its fluidity. Similar ultra-
252 stability of water in nanoscale spaces has also been reported inside carbon nanotubes [50,51].

253

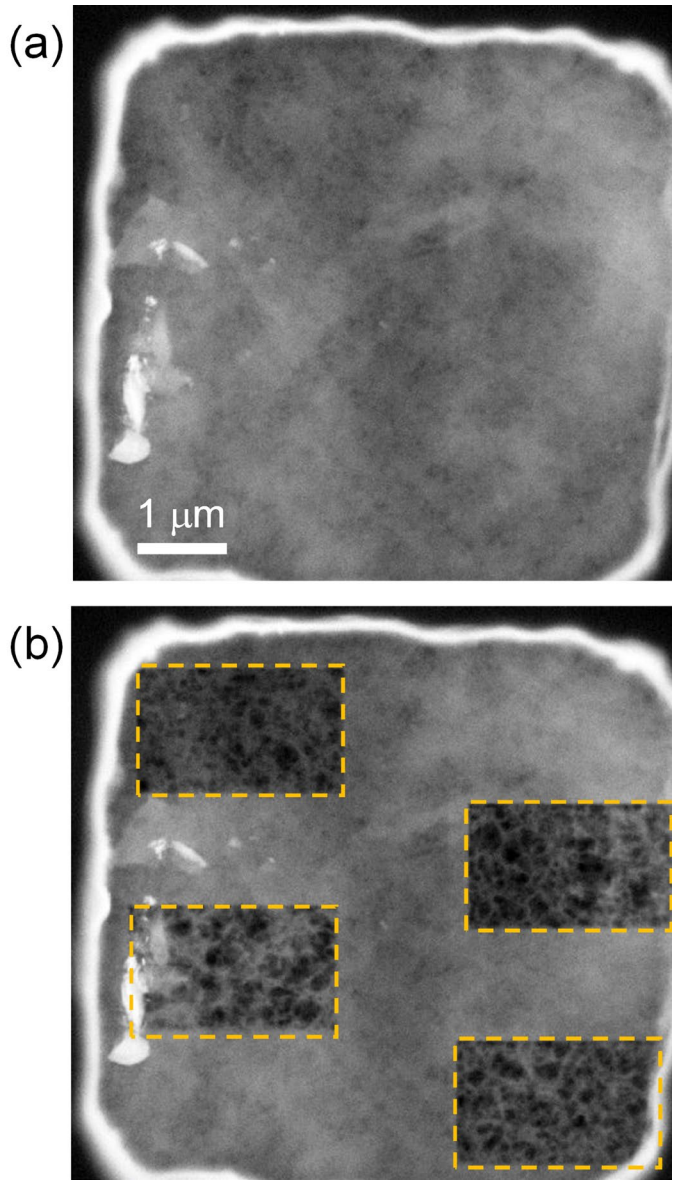

Fig. 3. ADF-STEM images of a water-retaining CNF film taken (a) before and (b) after radiolysis within the yellow dashed frames.

3.3 Wettability transition model of CNF films

On the basis of the above observations, we explain why the contact angle of thin CNF films varies and approaches that of the underneath substrate as the thickness decreases. Because CNF films exhibited

porous characteristics, a droplet placed on a surface gradually soaked into the film over time (as shown in Supplementary Material, Note 4). Through this soaking process, the bottom of the droplet can be in contact with three types of materials: the CNFs, water present within the fiber network, and the underlying substrate. Therefore, the contact angle is determined by the ratio of the areas of the three materials with which the droplet is in contact.

As shown in Fig. 1(c), when the mean thickness of the CNF film exceeded approximately 150 nm, the contact angle consistently remained around 20° regardless of the thickness. TEM observations revealed that in locally thick regions of the CNF film (corresponding to Fig. 2(a, b), the green frame of Fig. 2(c-d) and Fig. 3), the fibers were densely intertwined to form a 3D network structure capable of gelation by retaining water in nanoscale spaces. Thus, when the mean film thickness exceeds 150 nm, the entire film can be assumed to become thick regions (water-captured regions) as illustrated in Fig. 4(a). In such a case, the film adopts a gel-like structure, preventing wetting of the underlying silicon substrate due to its thickness. Therefore, the water droplet can be in contact with only two materials: CNFs and water captured in the fiber-network structure. Moreover, the contact angle of CNF films is determined by the area ratio of these materials. Assuming that their ratio is uniform all over the area, the contact angles should be constant on the thick gel-like film regardless of the film thickness.

On the other hand, when the mean thickness of the CNF film was lower than 150 nm or less, the contact angles tended to increase with the decrease in mean thickness, approaching that of the underlying substrate. As shown in Fig. 2(c-d), the CNF films were composed of thick regions (water-captured regions) and thin regions (non-captured regions) because of the nanoscale thickness distribution as

shown in Fig. 1(b). In the locally thin regions, the CNF network was sparse and did not retain water (see Supplementary Material, Note 3), leading to the water droplet wetting the underlying substrate. In other words, the thin regions are regarded as the composite surface of the pristine CNFs and the underlying substrate. Consequently, the film with a mean thickness of less than 150 nm becomes three composite surfaces consisting of CNFs, the silicon substrate, and retained water inside the CNF networks. As mean thickness decreases, the area of the thick regions (hydrogel regions) should decrease while the thin regions (non-captured regions) increase, approaching the wettability of the underlying substrate surface. Additionally, because individual fiber diameters vary within a range of 5.4 to 67.4 nm, even films with the same mean thickness may or may not form dense 3D networks. This variability in network formation is likely the reason for the dispersion of measured contact angles when the mean film thickness is less than 150 nm.

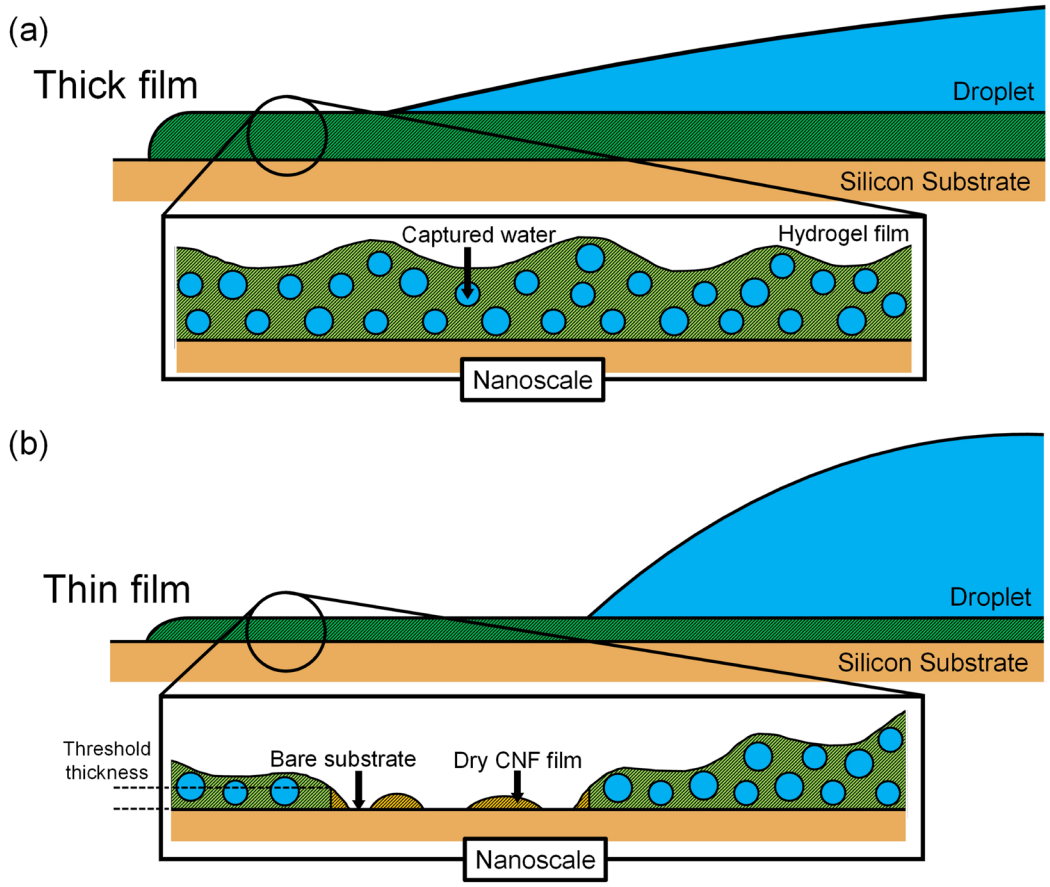

Fig. 4. Internal and surface structure of a (a) thick and (b) thin CNF film. An enlarged schematic diagram at the nanoscale is presented within the rectangular frame. CNFs are indicated by the black hatch pattern. The green region within the inset represents the hydrogel regions, while the orange regions correspond to the thin CNF film. The blue circle indicates water trapped within the thick film.

In this study, we disregarded the effect of differences in CNF's crystallinity on wettability for the following reasons. Generally, the interaction between CNFs and water is localized on the surfaces of the crystalline regions and the amorphous regions, which means that crystallinity could potentially influence wettability. According to the FTIR analysis (refer to Supplementary Material, Note 1), differences in crystallinity were observed between the thick and thin CNF films. However, during contact angle

measurements, water infiltration into the amorphous regions causes molecular reorientation, resulting in uniform crystallinity regardless of the film thickness. Therefore, the impact of crystallinity differences on surface wettability is assumed to be negligible in our experiments.

Moreover, we also disregarded the effects of time, humidity, and temperature on the wettability of CNF films for the two main reasons. First, the time-dependence induced by wicking and evaporation was eliminated by measuring contact angles after spreading was complete (refer to Supplementary Material, Note 5). Second, by standardizing the ambient conditions for these measurements, the effects of humidity and temperature on wettability become negligible (refer to Supplementary Material, Notes 6 and 7). In addition, the wettability can also be altered by the adsorption of volatile organic compounds (VOCs) in the ambient air due to the presence of substantial quantities of hydroxy groups. Yan et al. observed that CuO surfaces became hydrophobic after being exposed to the atmosphere, which was attributed to the adsorption of volatile organic compounds (VOCs) from the ambient air [41]. Their adsorption is inevitable because VOCs exist ubiquitously, but the timescale for the change in contact angle due to the adsorption is on the order of days [52]. Therefore, to minimize the effect of VOCs adsorption, all processes from sample preparation to contact angle measurement were carried out within a cleanroom environment, and the contact angle measurements were conducted immediately after the film formation.

3.4 Quantification of the area ratio

To quantitatively investigate the area ratio of the substances in contact with the droplet, the Cassie-Baxter equation was employed. In general, the Cassie-Baxter equation is considered applicable to Young's contact angle, which is shown on ideally uniform surfaces. However, in most cases, solid surfaces are not ideally uniform but rather exhibit heterogeneity. As a result, obtaining Young's contact angle under practical conditions proves to be challenging. Although the apparent contact angle does not fully reflect surface wettability, the application of the Cassie-Baxter equation is widely accepted as sufficiently feasible in many studies [53,54]. Second, the roughness factor of a CNF film, defined as the ratio of the actual area of a rough surface to the geometrically projected area, was calculated using CSI. It was found to be consistently around 1.01, regardless of film thickness. It is evident that the CNF film surface is extremely uniform and its roughness effect on the wettability is negligible. Therefore, in this study, it was assumed to be appropriate to use the Cassie-Baxter equation to represent the wetting characteristics of CNF films. The three types of materials contributing to the film's wetting are the silicon substrate, CNF fibers, and water trapped within the fiber network. The contact angle θ of the droplet on CNF films can be expressed as follows:

$$\cos\theta = A_{\mathrm{Si}}\cos\theta_{\mathrm{Si}} + A_{\mathrm{CNF}}\cos\theta_{\mathrm{CNF}} + A_{\mathrm{water}}\cos\theta_{\mathrm{water}} \quad (1)$$

$$A_{\mathrm{Si}} + A_{\mathrm{CNF}} + A_{\mathrm{water}} = 1 \quad (2)$$

A_{Si}, A_{CNF} and A_{water} and θ_{Si}, θ_{CNF} and θ_{water} represent the area ratios and contact angles of the silicon substrate, CNFs, and water, respectively. θ_{Si} was determined to be 80.3 ± 3.2° from the experiment, and θ_{water} was assumed to be 0°. A_{CNF} can also be expressed as $A_{\mathrm{CNF}} = A_{\mathrm{CNFthk}} + A_{\mathrm{CNFthn}}$, where A_{CNFthk} represents the ratio of CNFs in thick hydrogel films that can capture water inside, while A_{CNFthn} is the ratio for thin films that cannot. First, in the case that the mean film

thickness was much greater than 150 nm, A_{Si} and A_{CNFthn} could be assumed to be zero. Also, the ratio between A_{CNFthk} and A_{water} was determined to be $A_{\mathrm{CNFthk}}: A_{\mathrm{water}} = 0.68: 0.32$ from the atomic force microscopy (AFM) image of a binarized thick CNF film (see Supplementary Material, Note 8). Thus, by solving eq. (1) from these results, θ_{CNF} was determined to be 24.9°.

Next, we consider the area ratios of A_{Si}, A_{CNF}, and A_{water} when the CNF film is thin. To experimentally determine the area ratio of the underneath substrate (A_{Si}), the area of the exposed substrate was directly calculated by analyzing the local thickness distribution (histogram) of CNF films formed on a glass slide obtained by CSI (see Supplementary Material, Note 9). However, nanoscale voids in the films could not be measured by CSI due to the diffraction limit of the light (approximately 1 μm). To address this issue, the area ratio of the nanosopically exposed substrate was measured using AFM. Fig. S10 (see Supplementary Material, Note 10) shows the relationship between the mean film thickness and the substrate-exposed ratio calculated from the results of CSI and AFM. Based on this data, an empirical formula was obtained as $A_{\mathrm{Si}} = e^{-0.05T}$, where R-squared value was 0.93.

Fig. 5 illustrates the area ratio of the material in contact with the bottom of a droplet as a function of the mean film thickness, which is determined using eq. (1), (2), and the equation of $A_{\mathrm{Si}} = e^{-0.05T}$. It was observed that A_{water} reached zero at a thickness of 68 nm, suggesting that this value was the threshold where CNF films begin to locally transform into the hydrogel state. Consequently, A_{water} was assumed to be zero for thicknesses below 68 nm. This threshold thickness is reasonable because at least approximately twice the average diameter of individual fibers (37.2 nm) is needed to form three-

dimensional CNF networks capable of retaining water. Furthermore, an increase in A_{water} started at the threshold mean thickness of 68 nm and became approximately constant for mean thicknesses above around 150 nm, resulting in the value measured on a thick CNF film by AFM (0.32). On the other hand, as the mean thickness of films increased, A_{Si} decreased and converged to zero beyond a thickness of 150 nm. Conversely, A_{CNF} started to increase and reached its maximum at 68 nm, then gradually decreased and converged to the value of 0.68, as measured by AFM.

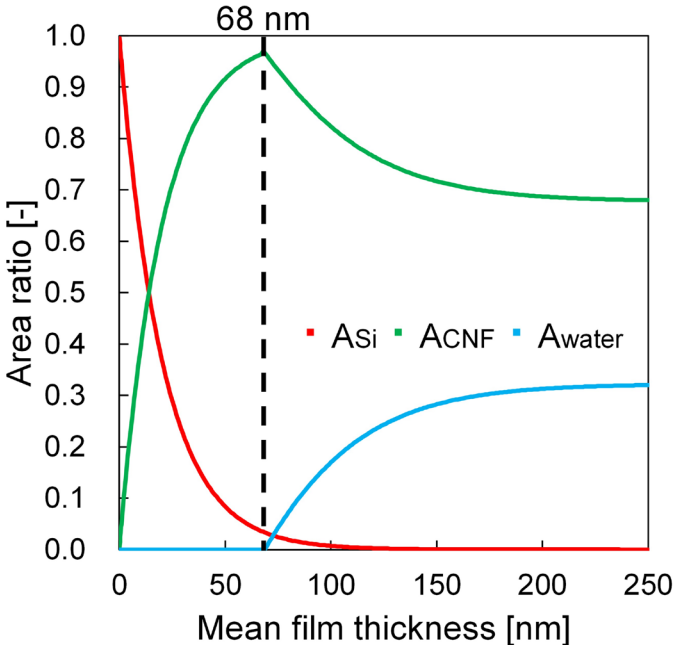

Fig. 5. The area ratio of the bottom of the water droplet contacting three different substances (the silicon substrate, CNFs, and captured water). The solid lines in red, green, and blue respectively represent the area ratios of the silicon substrate, CNFs, and water in contact. The dashed line indicates the threshold mean thickness at which water is retained in CNF films.

382 According to Fig. 5, we describe how the three different area ratios (A_{Si}, A_{CNF}, and A_{water}) change
383 with the mean film thickness. First, in the range of mean thickness from 0 to 68 nm, A_{Si} decreased as
384 the thickness increased. This is due to the denser spacing between fibers as observed by TEM (Fig. 2(a-
385 b) and Fig. 3), leading to a reduction in the exposed substrate. In contrast, A_{CNF} increased with
386 increasing thickness, resulting in a transition towards hydrophilicity. Moreover, the films could not
387 achieve the threshold thickness required for water retention, thus $A_{\mathrm{water}} = 0$ holds. Secondly, within
388 the mean thickness range of 68 to 150 nm, A_{CNF} started to decrease as the mean thickness increased.
389 This decrease is attributed to a rise in A_{water} due to the film's hydrogelation. Meanwhile, A_{Si}
390 continued to decrease and eventually reached zero, as also shown in Fig. S10. Lastly, when the mean
391 film thickness exceeds 150 nm, both A_{CNF} and A_{water} converged to constant values: 0.68 and 0.32,
392 respectively. This stabilization explains why the contact angles on the thick CNF film remained nearly
393 constant.

394

Conclusion

In this study, we investigated the wettability of CNF films deposited on silicon substrates. The results showed that the wettability of the film approached that of the underlying substrate as the mean film thickness decreased to below 150 nm. Our TEM observations also revealed that the CNFs formed dense 3D networks in thicker regions in which they retained water, whereas in thinner regions, the fiber density was low and the network structure was 2D. Thus, nanoscopically thin CNF films are expected to have both regions where water is captured and non-captured. From these results, we proposed a mechanism of the contact-angle dependence on the film thickness whereby the surface covered by a thin CNF film becomes a hybrid of the silicon substrate, CNFs, and water trapped in the gel region. Then, using the Cassie-Baxter equation, we quantitatively discussed the area ratio at the interfaces in contact with the bottom of the droplet contacts. Finally, the threshold thickness needed for local gelation was determined to be 68 nm. These findings will extend our fundamental knowledge about wetting behavior on CNF films and will be valuable for offering insights into potential applications like surface modification and functional coatings.

Declaration of Competing Interest

The authors declare that they have no known competing financial interests or personal relationships that could have appeared to influence the work reported in this paper.

CRediT authorship contribution statement

Masumi Misaka: Methodology, Formal analysis, Investigation, Writing – original draft, Visualization. **Hideaki Teshima**: Methodology, Validation, Resources, Writing – review & editing, Visualization, Funding acquisition. **Sota Hirokawa**: Investigation, Validation, Writing – review & editing. **Qin-Yi Li**: Resources, Writing – review & editing, Funding acquisition. **Koji Takahashi**: Conceptualization, Writing – review & editing, Supervision, Funding acquisition.

Data availability

Data will be made available on request.

Acknowledgments

This work was supported by JST CREST Grant No. JPMJCR18I1, JSPS KAKENHI Grant No. JP20H02089, JP21K20405, JP22K14193, and JP22K18772. The X-ray diffraction analysis and FT/IR

427 analysis were performed using SmartLab SE and FT/IR-6800, respectively, at the Center of Advanced
428 Instrumental Analysis, Kyushu University.

429

430 Appendix A. Supplementary Material

431 Supplementary Material to this article can be found online at xxxxx

432

433 References

434 [1] W. Liu, Y. Lu, Y. Shen, H. Chen, Y. Ni, Y. Xu, Spontaneous Transport Mechanics of Water
435 Droplets under a Synergistic Action of Designed Pattern and Non-Wetting Gradient, ACS
436 Omega. 8 (2023) 16450–16458. https://doi.org/10.1021/acsomega.3c01536.

437 [2] L. Wen, Y. Tian, L. Jiang, Bioinspired super-wettability from fundamental research to practical
438 applications, Angew. Chemie - Int. Ed. 54 (2015) 3387–3399.
439 https://doi.org/10.1002/anie.201409911.

440 [3] T. Watanabe, N. Yoshida, Wettability control of a solid surface by utilizing photocatalysis, Chem.
441 Rec. 8 (2008) 279–290. https://doi.org/10.1002/tcr.20154.

442 [4] X.M. Li, D. Reinhoudt, M. Crego-Calama, What do we need for a superhydrophobic surface? A
443 review on the recent progress in the preparation of superhydrophobic surfaces, Chem. Soc. Rev.
444 36 (2007) 1350–1368. https://doi.org/10.1039/b602486f.

[5] K. Yin, J. Wu, Q. Deng, Z. Wu, T. Wu, Z. Luo, J. Jiang, J.A. Duan, Tailoring micro/nanostructured porous polytetrafluoroethylene surfaces for dual-reversible transition of wettability and transmittance, Chem. Eng. J. 434 (2022) 134756. https://doi.org/10.1016/j.cej.2022.134756.

[6] W. Deng, G. Wang, L. Tang, Z. Zeng, T. Ren, One-step fabrication of transparent Barite colloid with dual superhydrophilicity for anti-crude oil fouling and anti-fogging, J. Colloid Interface Sci. 608 (2022) 186–192. https://doi.org/10.1016/j.jcis.2021.09.178.

[7] H. Zhao, C.A. Deshpande, L. Li, X. Yan, M.J. Hoque, G. Kuntumalla, M.C. Rajagopal, H.C. Chang, Y. Meng, S. Sundar, P. Ferreira, C. Shao, S. Salapaka, S. Sinha, N. Miljkovic, Extreme Antiscaling Performance of Slippery Omniphobic Covalently Attached Liquids, ACS Appl. Mater. Interfaces. 12 (2020) 12054–12067. https://doi.org/10.1021/acsami.9b22145.

[8] S. Sett, P. Sokalski, K. Boyina, L. Li, K.F. Rabbi, H. Auby, T. Foulkes, A. Mahvi, G. Barac, L.W. Bolton, N. Miljkovic, Stable Dropwise Condensation of Ethanol and Hexane on Rationally Designed Ultrascalable Nanostructured Lubricant-Infused Surfaces, Nano Lett. 19 (2019) 5287–5296. https://doi.org/10.1021/acs.nanolett.9b01754.

[9] Z. Shi, H. Zeng, Y. Yuan, N. Shi, L. Wen, H. Rong, D. Zhu, L. Hu, L. Ji, L. Zhao, X. Zhang, Constructing Superhydrophobicity by Self-Assembly of SiO2@Polydopamine Core-Shell Nanospheres with Robust Oil-Water Separation Efficiency and Anti-Corrosion Performance, Adv. Funct. Mater. 33 (2023) 1–11. https://doi.org/10.1002/adfm.202213042.

[10] Z. Xue, S. Wang, L. Lin, L. Chen, M. Liu, L. Feng, L. Jiang, A novel superhydrophilic and underwater superoleophobic hydrogel-coated mesh for oil/water separation, Adv. Mater. 23 (2011) 4270–4273. https://doi.org/10.1002/adma.201102616.

[11] C.G.J. Prakash, R. Prasanth, Approaches to design a surface with tunable wettability : a review on surface properties, J. Mater. Sci. 56 (2020) 108–135. https://doi.org/10.1007/s10853-020-05116-1.

[12] D. Hill, A.R. Barron, S. Alexander, Controlling the wettability of plastic by thermally embedding coated aluminium oxide nanoparticles into the surface, J. Colloid Interface Sci. 567 (2020) 45–53. https://doi.org/10.1016/j.jcis.2020.01.116.

[13] B. Wu, J. Lyu, C. Peng, D. Jiang, J. Yang, J. Yang, S. Xing, L. Sheng, Inverse infusion processed hierarchical structure towards superhydrophobic coatings with ultrahigh mechanical robustness, Chem. Eng. J. 387 (2020) 124066. https://doi.org/10.1016/j.cej.2020.124066.

[14] S.J. Kim, I.C. Bang, J. Buongiorno, L.W. Hu, Effects of nanoparticle deposition on surface wettability influencing boiling heat transfer in nanofluids, Appl. Phys. Lett. 89 (2006) 153107. https://doi.org/10.1063/1.2360892.

[15] M. Stepien, J.J. Saarinen, H. Teisala, M. Tuominen, M. Aromaa, J. Kuusipalo, J.M. Mäkelä, M. Toivakka, Adjustable wettability of paperboard by liquid flame spray nanoparticle deposition, Appl. Surf. Sci. 257 (2011) 1911–1917. https://doi.org/10.1016/j.apsusc.2010.09.025.

[16] M.L. Luo, J.Q. Zhao, W. Tang, C.S. Pu, Hydrophilic modification of poly(ether sulfone) ultrafiltration membrane surface by self-assembly of TiO 2 nanoparticles, Appl. Surf. Sci. 249 (2005) 76–84. https://doi.org/10.1016/j.apsusc.2004.11.054.

[17] V. Vatanpour, S.S. Madaeni, A.R. Khataee, E. Salehi, S. Zinadini, H.A. Monfared, TiO2 embedded mixed matrix PES nanocomposite membranes: Influence of different sizes and types of

nanoparticles on antifouling and performance, Desalination. 292 (2012) 19–29. https://doi.org/10.1016/j.desal.2012.02.006.

[18] L. Yan, Y.S. Li, C.B. Xiang, S. Xianda, Effect of nano-sized Al2O3-particle addition on PVDF ultrafiltration membrane performance, J. Memb. Sci. 276 (2006) 162–167. https://doi.org/10.1016/j.memsci.2005.09.044.

[19] J. Yang, X. Zhu, Thermo-responsive surface wettability on a pristine carbon nanotube film, Carbon N. Y. 49 (2010) 19–23. https://doi.org/10.1016/j.carbon.2010.08.033.

[20] L. Valentini, C. Cantalini, L. Lozzi, I. Armentano, J.M. Kenny, S. Santucci, Reversible oxidation effects on carbon nanotubes thin films for gas sensing applications, MATER. SCI. ENG., C. 23 (2003) 523–529. https://doi.org/10.1016/S0928-4931(02)00356-9.

[21] R. Beigmoradi, A. Samimi, D. Mohebbi-Kalhori, Fabrication of polymeric nanofibrous mats with controllable structure and enhanced wetting behavior using one-step electrospinning, Polymer (Guildf). 143 (2018) 271–280. https://doi.org/10.1016/j.polymer.2018.04.025.

[22] W. Cui, X. Li, S. Zhou, J. Weng, Degradation patterns and surface wettability of electrospun fibrous mats, Polym. Degrad. Stab. 93 (2008) 731–738. https://doi.org/10.1016/j.polymdegradstab.2007.12.002.

[23] X.Q. Wu, X. Wu, T.Y. Wang, L. Zhao, Y.B. Truong, D. Ng, Y.M. Zheng, Z. Xie, Omniphobic surface modification of electrospun nanofiber membrane via vapor deposition for enhanced anti-wetting property in membrane distillation, J. Memb. Sci. 606 (2020) 118075. https://doi.org/10.1016/j.memsci.2020.118075.

[24] J. Cui, F. Li, Y. Wang, Q. Zhang, W. Ma, C. Huang, Electrospun nanofiber membranes for wastewater treatment applications, Sep. Purif. Technol. 250 (2020) 117116. https://doi.org/10.1016/j.seppur.2020.117116.

[25] O. Arslan, Z. Aytac, T. Uyar, Superhydrophobic, Hybrid, Electrospun Cellulose Acetate Nanofibrous Mats for Oil/Water Separation by Tailored Surface Modification, ACS Appl. Mater. Interfaces. 8 (2016) 19747–19754. https://doi.org/10.1021/acsami.6b05429.

[26] Y.X. Huang, Z. Wang, D. Hou, S. Lin, Coaxially electrospun super-amphiphobic silica-based membrane for anti-surfactant-wetting membrane distillation, J. Memb. Sci. 531 (2017) 122–128. https://doi.org/10.1016/j.memsci.2017.02.044.

[27] S. Pacheco Benito, L. Lefferts, Wettability of carbon nanofiber layers on nickel foils, J. Colloid Interface Sci. 364 (2011) 530–538. https://doi.org/10.1016/j.jcis.2011.08.039.

[28] H. Kargarzadeh, J. Huang, N. Lin, I. Ahmad, M. Mariano, A. Dufresne, S. Thomas, A. Gałęski, Recent developments in nanocellulose-based biodegradable polymers, thermoplastic polymers, and porous nanocomposites, Prog. Polym. Sci. 87 (2018) 197–227. https://doi.org/10.1016/j.progpolymsci.2018.07.008.

[29] W. Zhang, Y. Zhang, J. Cao, W. Jiang, Improving the performance of edible food packaging films by using nanocellulose as an additive, Int. J. Biol. Macromol. 166 (2021) 288–296. https://doi.org/10.1016/j.ijbiomac.2020.10.185.

[30] J. Xu, D. Sagnelli, M. Faisal, A. Perzon, V. Taresco, M. Mais, C.V.L. Giosafatto, K.H. Hebelstrup, P. Ulvskov, B. Jørgensen, L. Chen, S.M. Howdle, A. Blennow, Amylose/cellulose

nanofiber composites for all-natural, fully biodegradable and flexible bioplastics, Carbohydr. Polym. 253 (2021) 117277. https://doi.org/10.1016/j.carbpol.2020.117277.

[31] C. Ao, W. Yuan, J. Zhao, X. He, X. Zhang, Q. Li, T. Xia, W. Zhang, C. Lu, Superhydrophilic graphene oxide@electrospun cellulose nanofiber hybrid membrane for high-efficiency oil/water separation, Carbohydr. Polym. 175 (2017) 216–222. https://doi.org/10.1016/j.carbpol.2017.07.085.

[32] X. Li, L. Yuan, R. Liu, H. He, J. Hao, Y. Lu, Y. Wang, G. Liang, G. Yuan, Z. Guo, Engineering Textile Electrode and Bacterial Cellulose Nanofiber Reinforced Hydrogel Electrolyte to Enable High-Performance Flexible All-Solid-State Supercapacitors, Adv. Energy Mater. 11 (2021) 1–11. https://doi.org/10.1002/aenm.202003010.

[33] X. Kang, P. Sun, S. Kuga, C. Wang, Y. Zhao, M. Wu, Y. Huang, Thin Cellulose Nanofiber from Corncob Cellulose and Its Performance in Transparent Nanopaper, ACS Sustain. Chem. Eng. 5 (2017) 2529–2534. https://doi.org/10.1021/acssuschemeng.6b02867.

[34] G. Rodionova, Ø. Eriksen, Ø. Gregersen, TEMPO-oxidized cellulose nanofiber films: Effect of surface morphology on water resistance, Cellulose. 19 (2012) 1115–1123. https://doi.org/10.1007/s10570-012-9721-5.

[35] Y. Jiang, X. Liu, Q. Yang, X. Song, C. Qin, S. Wang, K. Li, Effects of residual lignin on composition, structure and properties of mechanically defibrillated cellulose fibrils and films, Cellulose. 26 (2019) 1577–1593. https://doi.org/10.1007/s10570-018-02229-4.

[36] H.J. Kim, S. Roy, J.W. Rhim, Effects of various types of cellulose nanofibers on the physical properties of the CNF-based films, J. Environ. Chem. Eng. 9 (2021) 106043. https://doi.org/10.1016/j.jece.2021.106043.

[37] X. Sun, C. Mei, A.D. French, S. Lee, Y. Wang, Q. Wu, Surface wetting behavior of nanocellulose-based composite films, Cellulose. 25 (2018) 5071–5087. https://doi.org/10.1007/s10570-018-1927-8.

[38] W. Li, Y. Wu, W. Liang, B. Li, S. Liu, Reduction of the Water Wettability of Cellulose Film through Controlled Heterogeneous Modi fi cation, ACS Appl. Mater. Interfaces. 6 (2014) 5726–5734.

[39] J. Cai, Q. Chen, C. Chang, Spray-assisted LBL assembly of chitosan/nanocellulose as coatings of commercial membranes for oil-in-water emulsion separation, Int. J. Biol. Macromol. 242 (2023) 124852. https://doi.org/10.1016/j.ijbiomac.2023.124852.

[40] N. Jamaluddin, Y.I. Hsu, T.A. Asoh, H. Uyama, Effects of acid-anhydride-modified cellulose nanofiber on poly(Lactic acid) composite films, Nanomaterials. 11 (2021) 1–15. https://doi.org/10.3390/nano11030753.

[41] X. Yan, Z. Huang, S. Sett, J. Oh, H. Cha, L. Li, L. Feng, Y. Wu, C. Zhao, D. Orejon, F. Chen, N. Miljkovic, Atmosphere-mediated superhydrophobicity of rationally designed micro/nanostructured surfaces, ACS Nano. 13 (2019) 4160–4173. https://doi.org/10.1021/acsnano.8b09106.

[42] T. Huhtamäki, X. Tian, J.T. Korhonen, R.H.A. Ras, Surface-wetting characterization using contact-angle measurements, Nat. Protoc. 13 (2018) 1521–1538. https://doi.org/10.1038/s41596-018-0003-z.

[43] X.M. Yang, Z.W. Zhong, E.M. Diallo, Z.H. Wang, W.S. Yue, Silicon wafer wettability and aging behaviors: Impact on gold thin-film morphology, Mater. Sci. Semicond. Process. 26 (2014) 25–32. https://doi.org/10.1016/j.mssp.2014.03.044.

[44] N.M. Schneider, M.M. Norton, B.J. Mendel, J.M. Grogan, F.M. Ross, H.H. Bau, Electron-Water interactions and implications for liquid cell electron microscopy, J. Phys. Chem. C. 118 (2014) 22373–22382. https://doi.org/10.1021/jp507400n.

[45] S. Hirokawa, H. Teshima, P. Solís-Fernández, H. Ago, Y. Tomo, Q.Y. Li, K. Takahashi, Nanoscale Bubble Dynamics Induced by Damage of Graphene Liquid Cells, ACS Omega. 5 (2020) 11180–11185. https://doi.org/10.1021/acsomega.0c01207.

[46] S. Nag, Y. Tomo, H. Teshima, K. Takahashi, M. Kohno, Dynamic interplay between interfacial nanobubbles: oversaturation promotes anisotropic depinning and bubble coalescence, Phys. Chem. Chem. Phys. 23 (2021) 24652–24660. https://doi.org/10.1039/d1cp03451k.

[47] J.M. Grogan, N.M. Schneider, F.M. Ross, H.H. Bau, Bubble and pattern formation in liquid induced by an electron beam, Nano Lett. 14 (2014) 359–364. https://doi.org/10.1021/nl404169a.

[48] J. Park, K. Koo, N. Noh, J.H. Chang, J.Y. Cheong, K.S. Dae, J.S. Park, S. Ji, I.D. Kim, J.M. Yuk, Graphene Liquid Cell Electron Microscopy: Progress, Applications, and Perspectives, ACS Nano. 15 (2021) 288–308. https://doi.org/10.1021/acsnano.0c10229.

[49] S. Hirokawa, H. Teshima, P. Solís-Fernández, H. Ago, Q.Y. Li, K. Takahashi, Pinning in a Contact and Noncontact Manner: Direct Observation of a Three-Phase Contact Line Using Graphene Liquid Cells, Langmuir. 37 (2021) 12271–12277. https://doi.org/10.1021/acs.langmuir.1c01589.

[50] Q.Y. Li, R. Matsushita, Y. Tomo, T. Ikuta, K. Takahashi, Water Confined in Hydrophobic Cup-Stacked Carbon Nanotubes beyond Surface-Tension Dominance, J. Phys. Chem. Lett. 10 (2019) 3744–3749. https://doi.org/10.1021/acs.jpclett.9b00718.

[51] Y. Tomo, A. Askounis, T. Ikuta, Y. Takata, K. Sefiane, K. Takahashi, Superstable Ultrathin Water Film Confined in a Hydrophilized Carbon Nanotube, Nano Lett. 18 (2018) 1869–1874. https://doi.org/10.1021/acs.nanolett.7b05169.

[52] J. Oh, D. Orejon, W. Park, H. Cha, S. Sett, Y. Yokoyama, V. Thoreton, Y. Takata, N. Miljkovic, The apparent surface free energy of rare earth oxides is governed by hydrocarbon adsorption, IScience. 25 (2022) 103691. https://doi.org/10.1016/j.isci.2021.103691.

[53] Y. Jiang, C.H. Choi, Droplet Retention on Superhydrophobic Surfaces: A Critical Review, Adv. Mater. Interfaces. 8 (2021) 1–26. https://doi.org/10.1002/admi.202001205.

[54] H.J. Butt, J. Liu, K. Koynov, B. Straub, C. Hinduja, I. Roismann, R. Berger, X. Li, D. Vollmer, W. Steffen, M. Kappl, Contact angle hysteresis, Curr. Opin. Colloid Interface Sci. 59 (2022) 101574. https://doi.org/10.1016/j.cocis.2022.101574.

List of figure captions

Fig. 1. (a) Photograph of a CNF film formed on a silicon substrate. (b) Thickness distribution of a CNF film with a mean thickness of 37.8 nm measured by CSI. (c) Relationship between the mean thicknesses

and contact angles of CNF films. The red dashed lines show the water contact angle on the pristine silicon substrate. The blue solid lines represent an empirical formula: $\theta = 59.8e^{-0.03T} + 20.5$. An enlarged view of the region of low mean thickness is shown as an inset.

Fig. 2. (a, b) Time series of radiolysis of water captured in CNF networks observed by TEM. (c, d) Time series of a CNF film composed of thin and thick regions. The regions in the red and green squares correspond to the thin and thick regions, respectively.

Fig. 3. ADF-STEM images of a water-retaining CNF film taken (a) before and (b) after radiolysis within the yellow dashed frames.

Fig. 4. Internal and surface structure of a (a) thick and (b) thin CNF film. An enlarged schematic diagram at the nanoscale is presented within the rectangular frame. CNFs are indicated by the black hatch pattern. The green region within the inset represents the hydrogel regions, while the orange regions correspond to the thin CNF film. The blue circle indicates water trapped within the thick film.

Fig. 5. The area ratio of the bottom of the water droplet contacting three different substances (the silicon substrate, CNFs, and captured water). The solid lines in red, green, and blue respectively represent the area ratios of the silicon substrate, CNFs, and water in contact. The dashed line indicates the threshold mean thickness at which water is retained in CNF films.